Supplementary Information (SI) for Lab on a Chip.

Supplementary Information

A Microfluidic Hanging Droplet as a Programmable Platform for Mammalian Egg Vitrification

Haidong Feng[a*+], Georgios Katsikis[b*‡], India Napier[c#], Gong Du[c], Josh Lim[d], Joseph O Doyle[d], Scott R Manalis[abe] and Linda G Griffith**[a]

[a] Department of Biological Engineering, Massachusetts Institute of Technology, Cambridge, Massachusetts 02139, United States
[b] Koch Institute for Integrative Cancer Research, Massachusetts Institute of Technology, Cambridge, Massachusetts 02139, United States
[c] Division of Comparative Medicine, Massachusetts Institute of Technology, Cambridge, Massachusetts 02139, United States
[d] Shady Grove Fertility Reproductive Science Center, Rockville, Maryland, 20850, United States
[e] Department of Mechanical Engineering, Massachusetts Institute of Technology, Cambridge, Massachusetts 02139, United States

[*]These authors contributed equally
[**] Corresponding author
[+]Present address: Zymeron Corporation, Durham, NC 27709, United States
[‡] Present address: Anthology Biotechnologies, Cambridge, MA 02139, United States
[#] Present address: Department of Comparative Pathobiology, Tufts University, N. Grafton, MA, 01536, United States

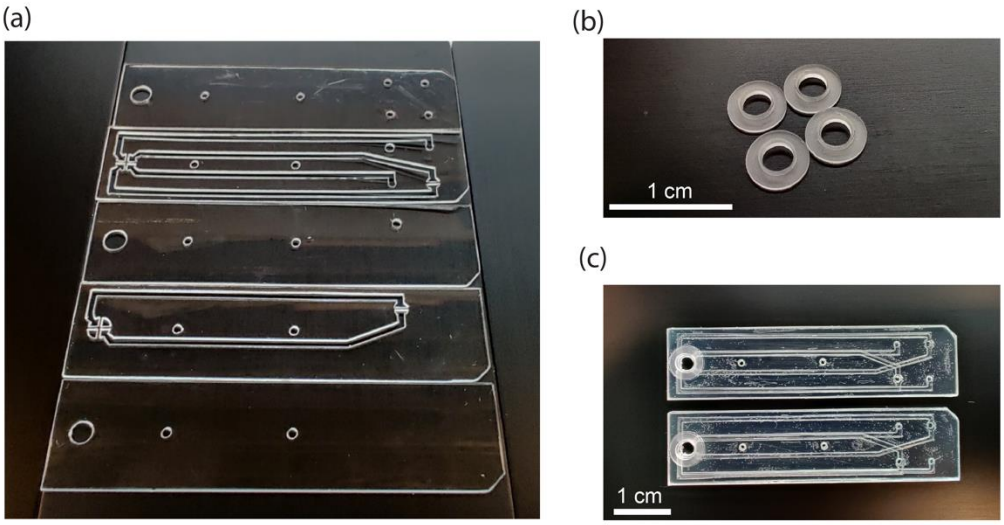

Fig. S1 Fabrication process of microfluidic chip. a) Two layers of microfluidic channels and three layers of cover (Fig. 1b, c) are patterned by cutting 250 µm-thick sheets of Cyclic Olefin Copolymer (COC) using vinyl cutter (Materials and Methods). b) Rims are fabricated from COC via CNC milling. c) The five layers get bonded together via thermal lamination. Rims get bonded with microfluidic chip utilizing COC elastomer E140 as adhesive layer.

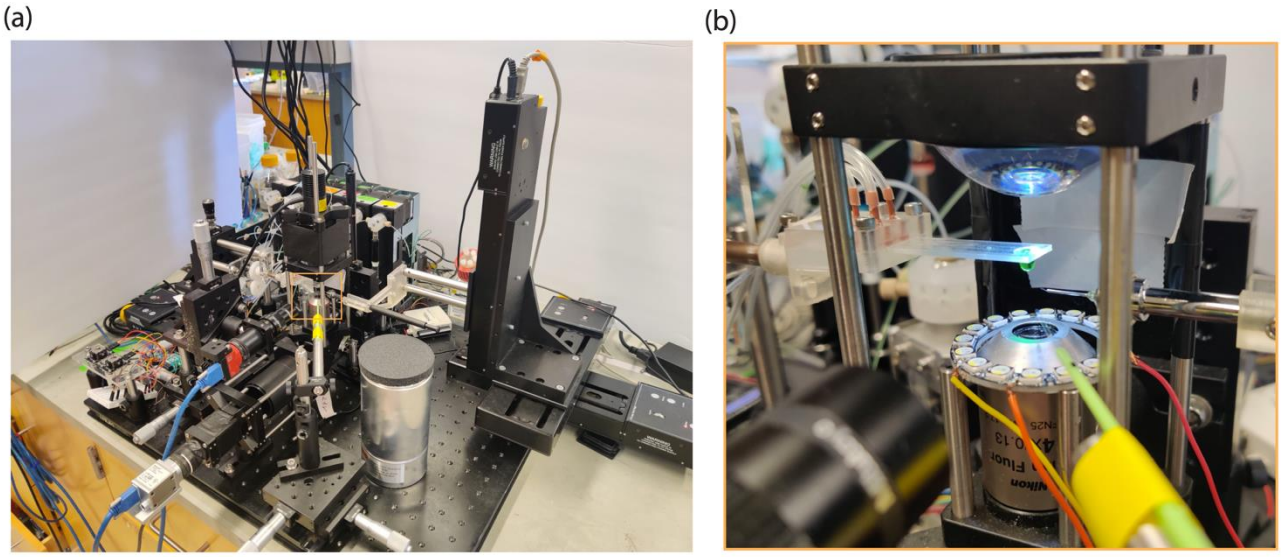

Fig. S2 Integrated platform for vitrification. a) Picture of set-up (Fig. 2) showing syringe pumps, video cameras, motorized stages and tank for liquid nitrogen. Orange rectangle denotes location of microfluidic chip b) Zoomed in picture of set-up corresponding to orange rectangle in (a), showing microfluidic chip with hanging droplet, the two objectives and the cryoloop as the main vitrification carrier. On the foreground, a cryotop is shown as an alternative vitrification carrier.

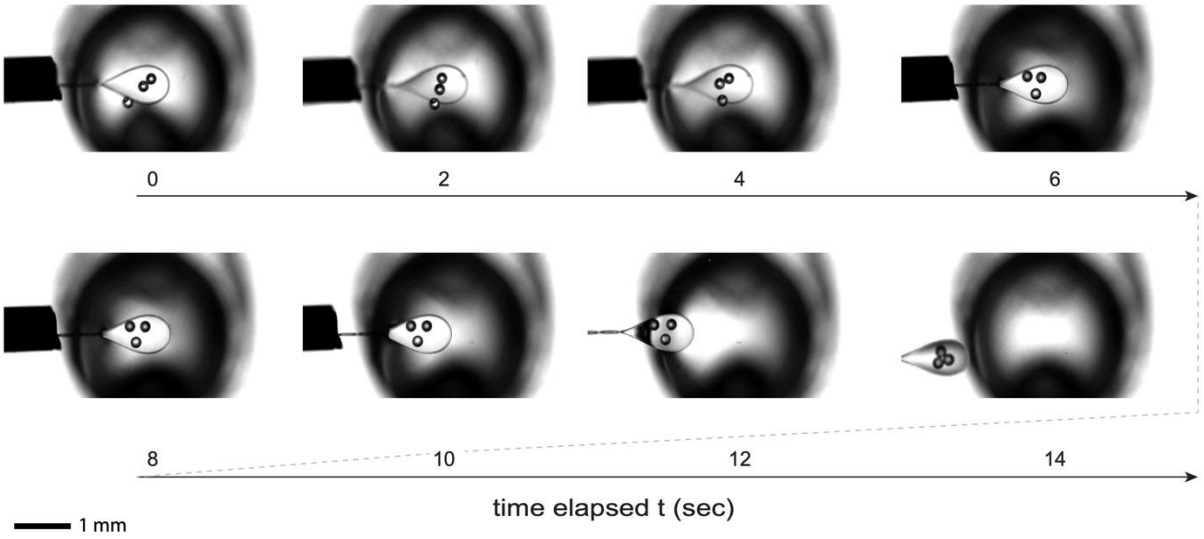

Fig S3 Proof-of-principle experiments for manually unloading particles from hanging droplet using Cryoloop. Demonstration of unloading polystyrene particles (150 µm diameter) from hanging drop utilizing Cryoloop. Images are taken from the bottom view of the hanging drop. When Cryoloop touches the water surface, water molecules attach to the Nylon wire, causing deformation of the surface. Beads pop out from the surface due to the surface deformation. By manually changing the Cryoloop position, particles can be captured within the loop. When the Cryoloops exit the liquid-air interface of the hanging droplet, particles get closed packed together in a liquid film retrieved from hanging drop. In order to minimize surface area, only a small fraction of liquid gets transferred onto the Cryoloop.

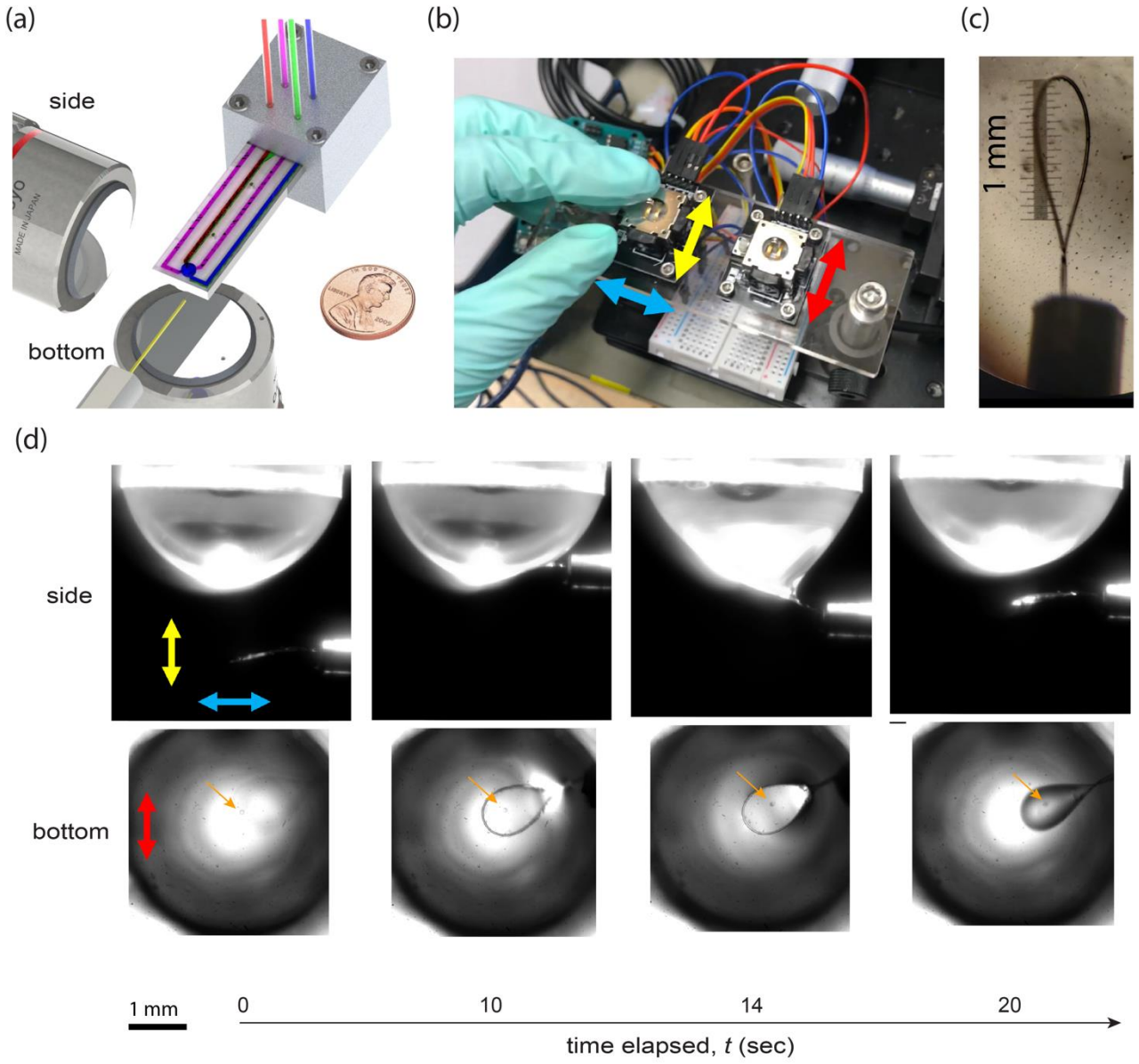

Fig. S4 Motorized System for unloading the egg from hanging droplet. a) CAD schematic of microfluidic chip in full assembly, showing two objectives for imaging hanging droplet from both side and bottom. A one-cent (diameter ~19mm) denotes the scale. b) Picture of double-joystick system (SMAKN Fr4 Ky-023) connected to microcontroller (Arduino). The colored arrows indicate the three directions of the joystick for moving the cryoloop in three dimensions in space (Fig. 2c). c) Picture of cryoloop with length scale from microscope objective. d) Test experiment for unloading a mouse egg from hanging droplet by using the joystick (Video S1) (b) and the side and bottom view imaging of the two objectives (a). The three big arrows correspond to the direction of motion by same-color arrows in (b) and the small arrows in orange indicate the position of egg. The objective and camera obtaining the bottom view resolve the morphology of eggs (Fig. 7b).

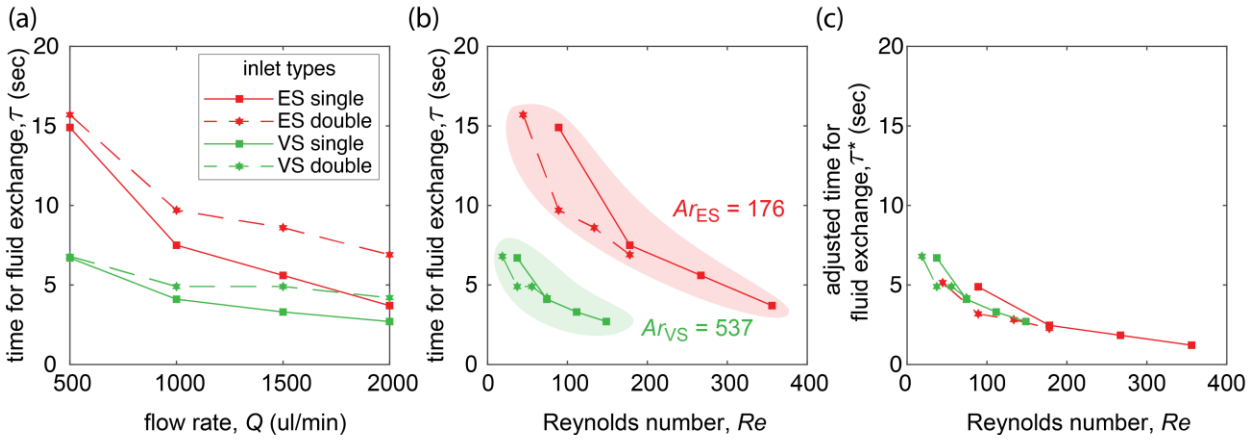

Fig S5 Analysis of flow regimes for cryoprotectant loading. a) COMSOL Simulations of time scales τ for liquid exchange for Equilibration Solution (ES, red) and Vitrification Solution (VS, green) for both single and double inlet types (squares vs asterisks). The τ are calculated as in **Figs. 5, S6**. b) Time scales vs Reynolds number expressing the ratio of inertial over viscous forces, and calculated as $Re = \rho V_a L/\mu$, with $V_a = Q/A$ (**Fig. 1e**) where $A = A_s$ for single inlets and $A = A_d = 2A_s$ for double inlets, using fluid properties (**Table.1**). The colored islands denote distinct flow regimes for ES and VS flows based on Archimedes number expressing the ratio of buoyant (or gravitational) over viscous forces, and calculated as $Ar = gL^3\rho_1(\rho_2 - \rho_1)/\mu^2$. For ES loading, we took $\rho_2 = \rho_{ES}$, $\rho_1 = \rho_{BS}$ and $\mu = \mu_{ES}$. For VS loading $\rho_2 = \rho_{VS}$, $\rho_1 = \rho_{ES}$ and $\mu = \mu_{VS}$ and typical length scale L from main text. We observe that ES loading happens at higher inertial/viscous (Re) forces and lower buoyancy/viscous (Ar) forces than VS, the cumulative result of which are longer times τ for liquid exchange than those for VS. c) Adjusted time scales $\tau^* = \tau\, Ar_i/Ar_{VS}$, where $i = ES$ and $i = VS$ respectively for ES and VS flows. The similar adjusted time scales τ^* between ES and VS suggest that there is a dominant buoyancy-driven effect in liquid exchange at lower Re regimes ($Re < 150$), while for higher Re ($Re > 150$) inertial forces have a greater role determining liquid exchange.

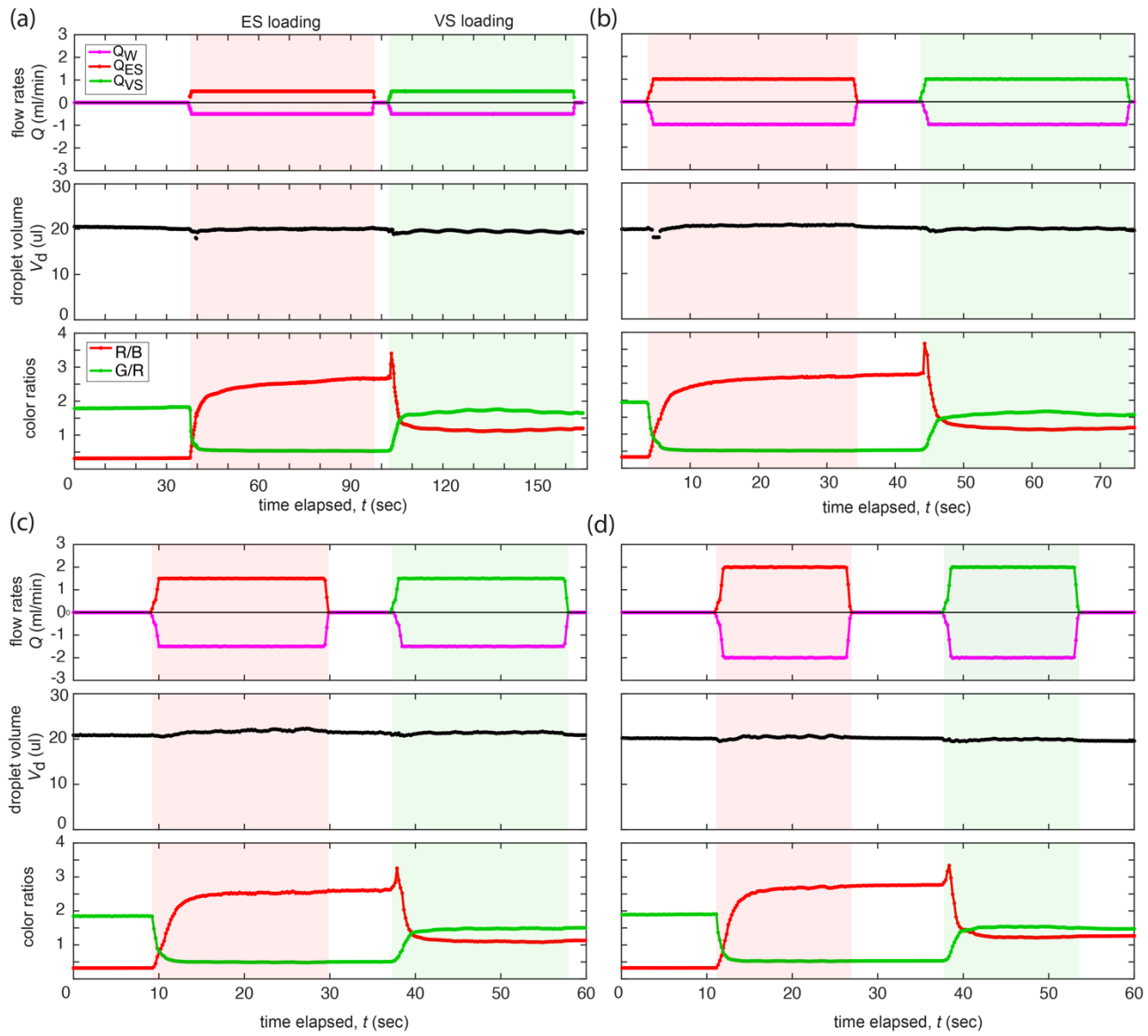

Fig. S6 Experimental characterization of flow control, droplet stability and liquid exchange. a-d) Four experiments for respectively flow rates of Q= 500,1,000, 1,500 and 2,000 µl/min. In each panel, top graph shows Q over time for equilibration solution (Q_{ES}), vitrification solution (Q_{VS}) sequentially dispensed (Q>0) into hanging droplet. To keep a constant droplet volume whenever Q_{ES} or Q_{VS} flow, an equal amount of flow rate Q_W is aspirated (Q<0) from hanging droplet into waste (**Video S3**). Red and green bands respectively denote activation of pumps for ES and VS loading. Middle graph shows corresponding droplet volume over time during liquid exchange measured using image analysis (Methods). Bottom graph Ratio of colors measured (Materials and Methods), where BS, ES and VS are respectively stained by blue, red and green color dye. Panel d is the same as **Fig. 4**.

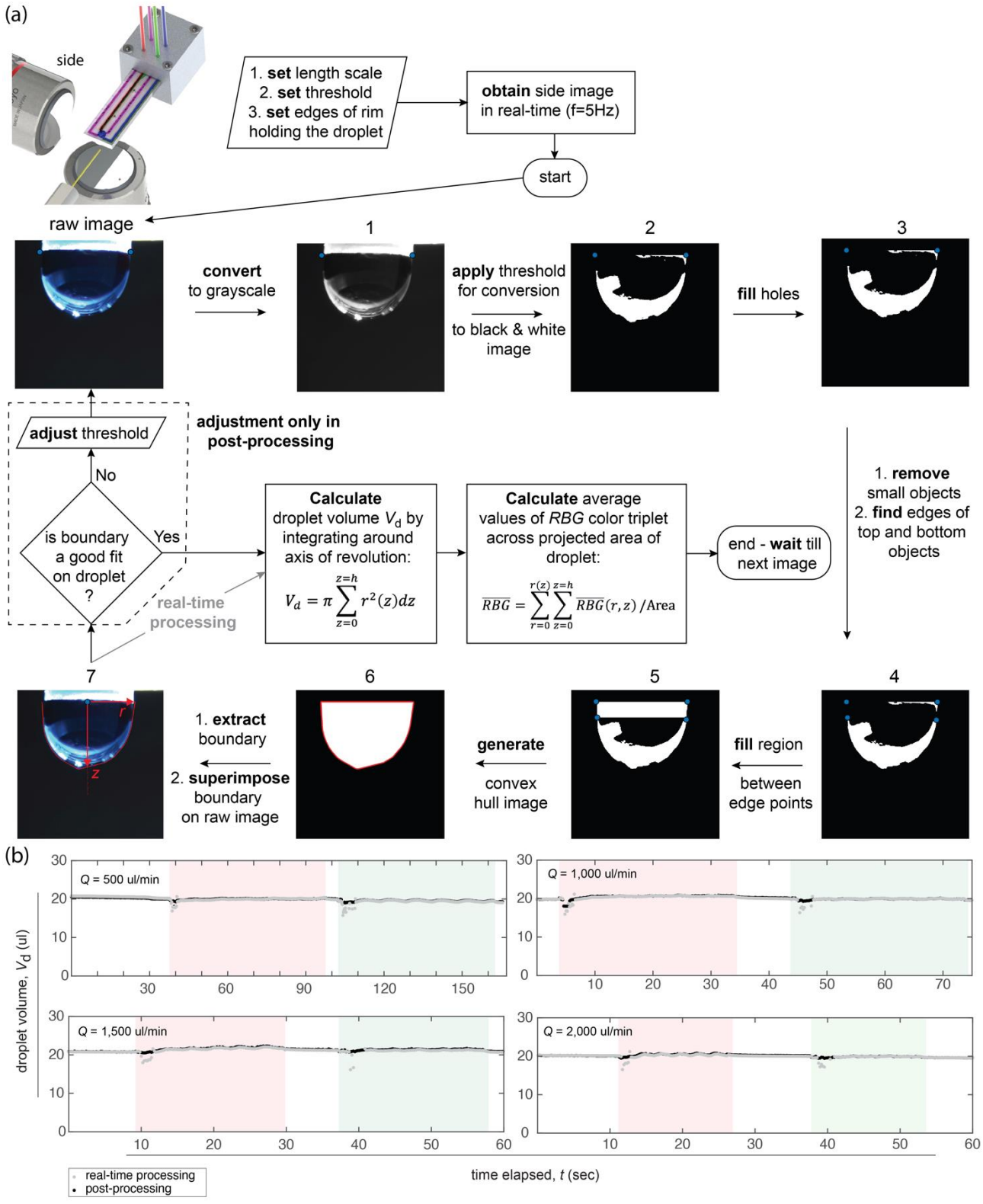
(a)
side
1. set length scale
2. set threshold
3. set edges of rim holding the droplet
obtain side image in real-time (f=5Hz)
start
raw image
1
convert to grayscale
2
apply threshold for conversion
to black & white image
3
fill holes
adjust threshold
adjustment only in post-processing
No
is boundary a good fit on droplet ?
Yes
real-time processing
Calculate droplet volume V_d by integrating around axis of revolution:
$V_d = \pi \sum_{z=0}^{z=h} r^2(z)dz$
Calculate average values of RBG color triplet across projected area of droplet:
$\overline{RBG} = \sum_{r=0}^{r(z)} \sum_{z=0}^{z=h} \overline{RBG}(r,z) / \text{Area}$
end - wait till next image
1. remove small objects
2. find edges of top and bottom objects
7
r
z
1. extract boundary
2. superimpose boundary on raw image
6
generate
convex hull image
5
fill region
between edge points
4
(b)
Q = 500 ul/min
Q = 1,000 ul/min
Q = 1,500 ul/min
Q = 2,000 ul/min
droplet volume, V_d (ul)
time elapsed, t (sec)
real-time processing
post-processing

Fig. S7 Brightness-thresholding algorithm for size and color calculation of droplet. a) The algorithm calculates the droplet volume in real time using the side view image at sampling rate of $f = 5\ Hz$ (top) after the user sets a threshold value. Then, the real-time algorithm implemented in LabVIEW Vision Development Module processes the raw image in seven steps. After the completion of these steps, the boundary of the droplet is superimposed on the image in real-time for monitoring by the user. If a single binary object is detected, the algorithm calculates the droplet volume V_d and mean $\overline{RGB}$ colors across the projected area. Otherwise, algorithm returns zero values for V_d and $\overline{RGB}$. To evaluate the efficiency of the real-time algorithm, the data were post-processed using a custom code in MATLAB that performs the same steps in addition to a visual check (area with dashed outline) that enables to user to adjust the threshold if the superimposed boundary is not a good fit or a single binary object is not detected. b) Comparison of V_d over time during ES and VS loading for four flow rates calculated in real-time processing vs post-processing (**Figs. 4, S6**). The real-time algorithm has an error of 20% only when droplet color changes (i.e. ES and VS loading). In some cases, the algorithm returns zero values for V_d. The accuracy of the real-time algorithm can be improved in the future by incorporating real-time automated adjustment of threshold using more advanced machine vision techniques.

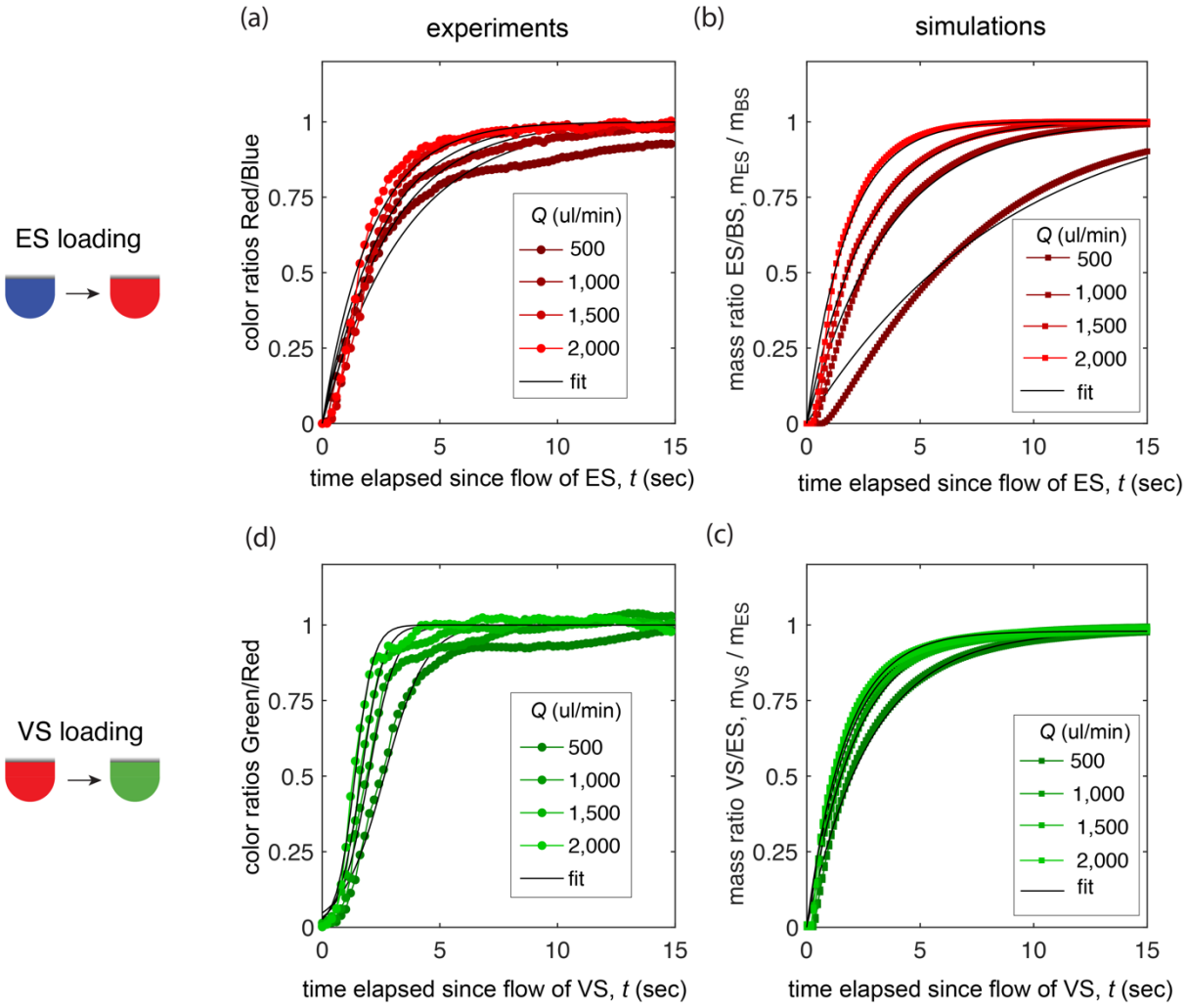

Fig. S8 Characterization of time scales for liquid exchange in handing droplet. a,b) Characterization of liquid exchange in ES loading using color ratio (Red/Blue) and mass ratio are respectively used for experiments (**Figs. 4, S6**) and simulations (**Fig. 3c,f**) for Q=500-2,000 μl/min. Each curve is normalized by steady-state value as determined by sigmoid fit for experiments and exponential fit for simulations. We calculated the time scale τ for liquid exchange as time needed to reach 90% of steady-state value (**Fig. 5**). c,d) Characterization of liquid exchange in VS loading with same notations as in a,b.

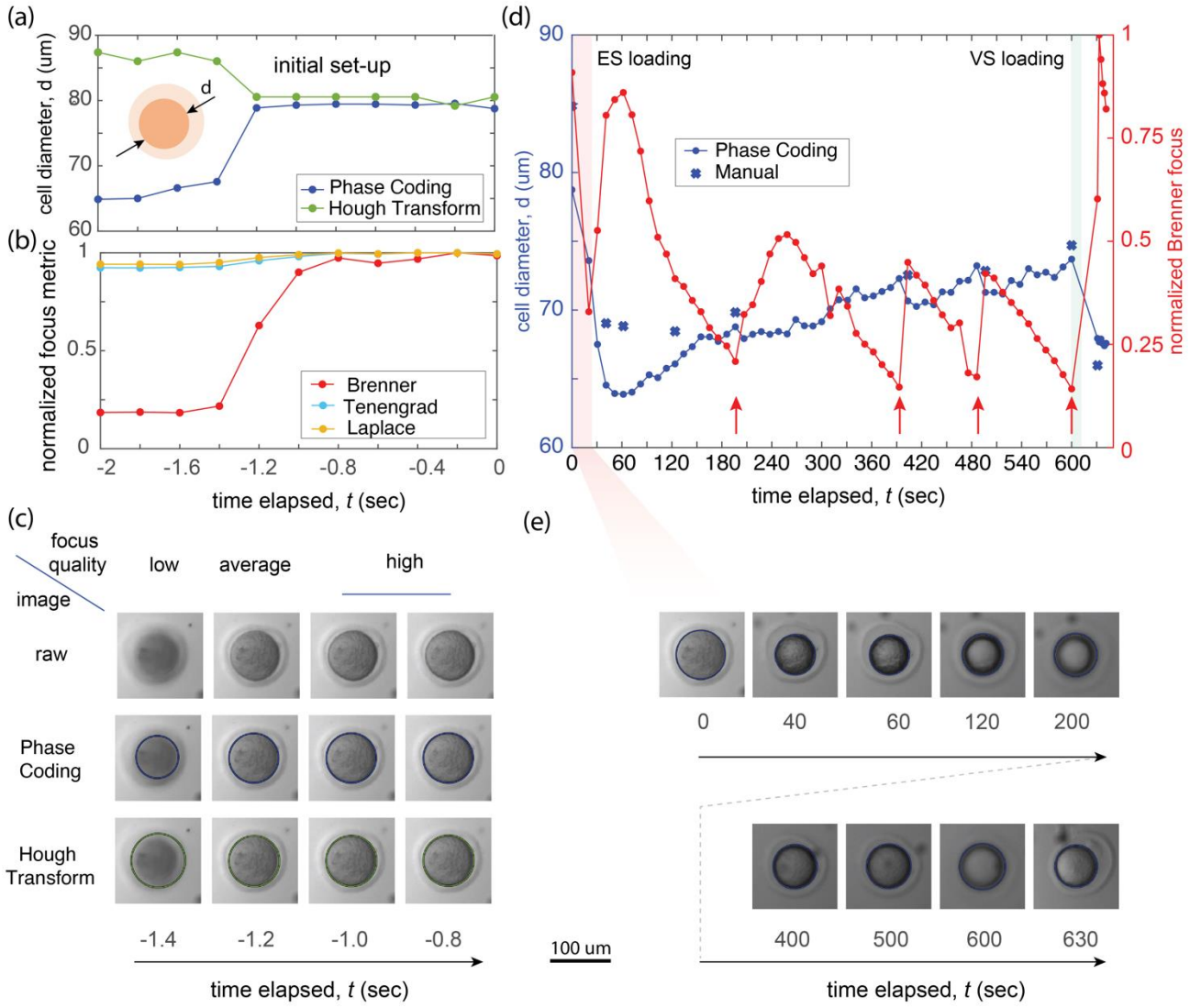

Fig. S9 Quantification of the effect of image focus on cell size measurement. a) Cell diameter over time during initial set-up for adjustment of focus. We calculated cell size using two methods that both yield 20% relative error when the image is out of focus (c). b) Focus metrics over time, normalized by maximum value for each metric for same dataset as in (a) and (c). The Brenner metric had the highest sensitivity for reporting on images of lower focus. c) Corresponding cell images for dataset of (a) and (b), including superposition of calculated cell diameter for two methods. d) Cell diameter and Brenner focus over time for entire experiment of ES and VS loading. We used Phase Coding and Brenner focus as the most reliable metrics. In the current platform the focus can be temporarily lost in short intervals of ES and VS loading (~10 sec) or drift, which is recovered by adjustment of the focus by the user using the motorized stage (action denoted by red arrows). While out-of-focus images (e) induce noise for size calculation, we can rely on the shape of the overall curve to extract the trend (i.e. size is increasing during equilibration). Notably, the manual size-estimation method (crosses) despite errors also captures similar trend as the Phase Coding (squares). Thus, we relied on the manual size-estimation method for reporting cell size trend on the population level (**Fig. 7a**).

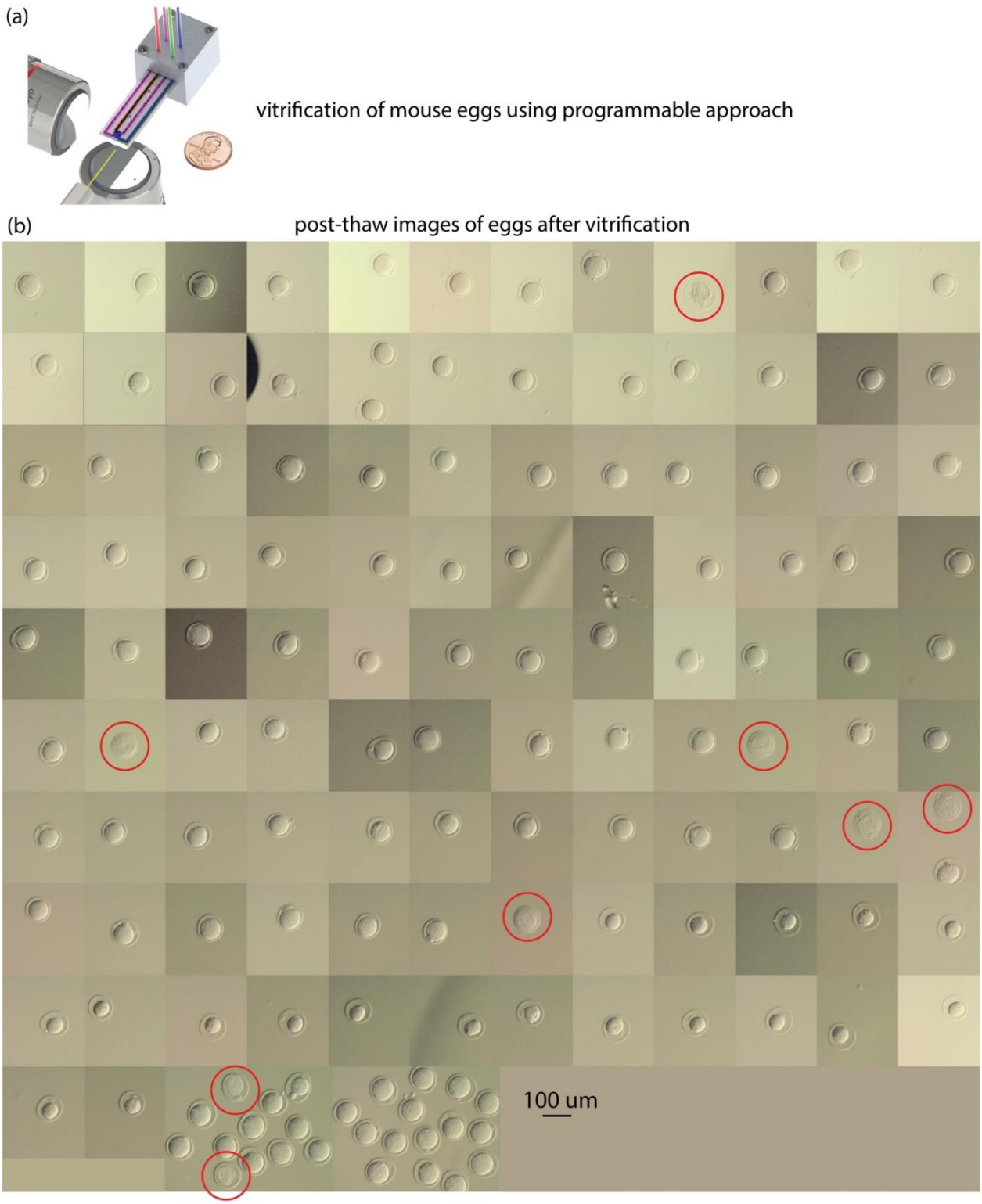

Fig. S10 Determination of percentage of post-thaw survival of eggs after vitrification using programmable approach. a) CAD schematic indicating automated approach (**Figs. 2, 6a,b, Video S4**). b) Images of eggs, where n=157 eggs were vitrified, n=139 were recovered in thawing and n=131 were considered alive post-thawing by observation of their morphology. Live eggs have a uniform cytoplasmic texture, while dead eggs have granular or heterogeneous cytoplasm. Red circles indicate dead cells.

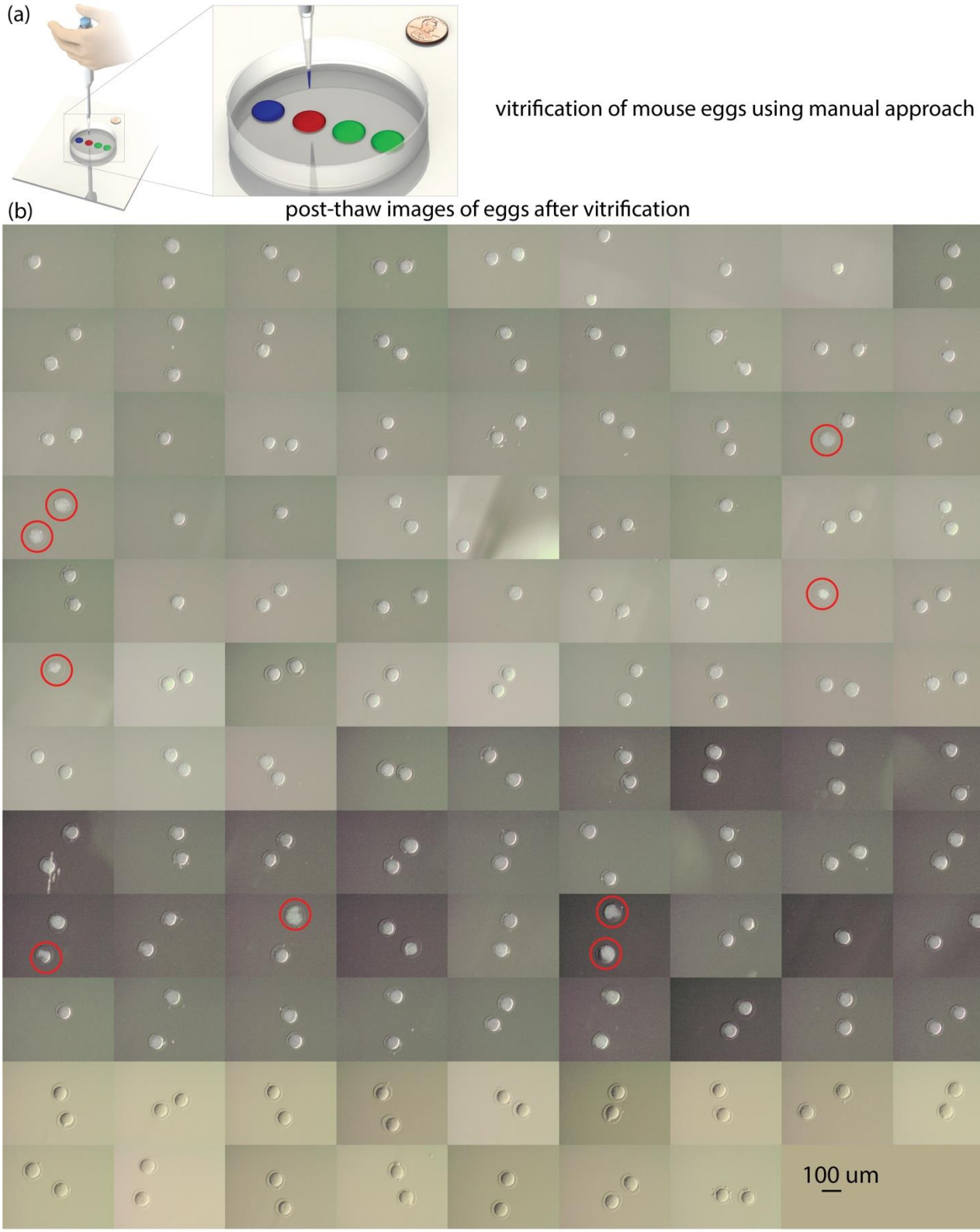

Fig. S11 Determination of percentage of post-thaw survival of eggs after vitrification using manual approach. a) CAD schematic indicating manual approach (**Figs. 2, 6c,d**). b) Images of eggs, where n=222 eggs were vitrified, n=196 were recovered in thawing and n=187 were considered alive post-thawing by observation of their morphology. Live eggs have a uniform cytoplasmic texture, while dead eggs have granular or heterogeneous cytoplasm. Red circles indicate dead cells.

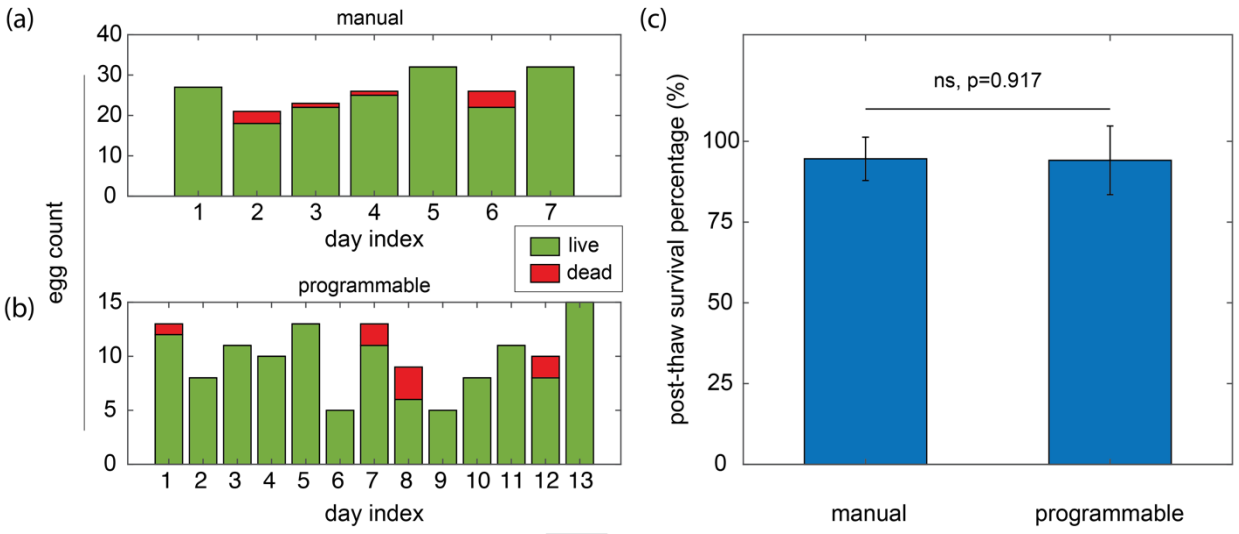

Fig. S12 Statistical comparison between manual and programmable vitrification approaches. a,b) Egg counts from manual (**Fig. S10**) and programmable (**Fig. S11**) vitrifications. Each replicate used oocytes extracted from healthy mice the same day. c) Bar graphs of mean values of ratio of live over total count of eggs for each day. Comparison is two-sample t-test where ns denotes non-significant differences with equal mean values and p-value of 0.917. Error bars indicate standard deviation between different days.

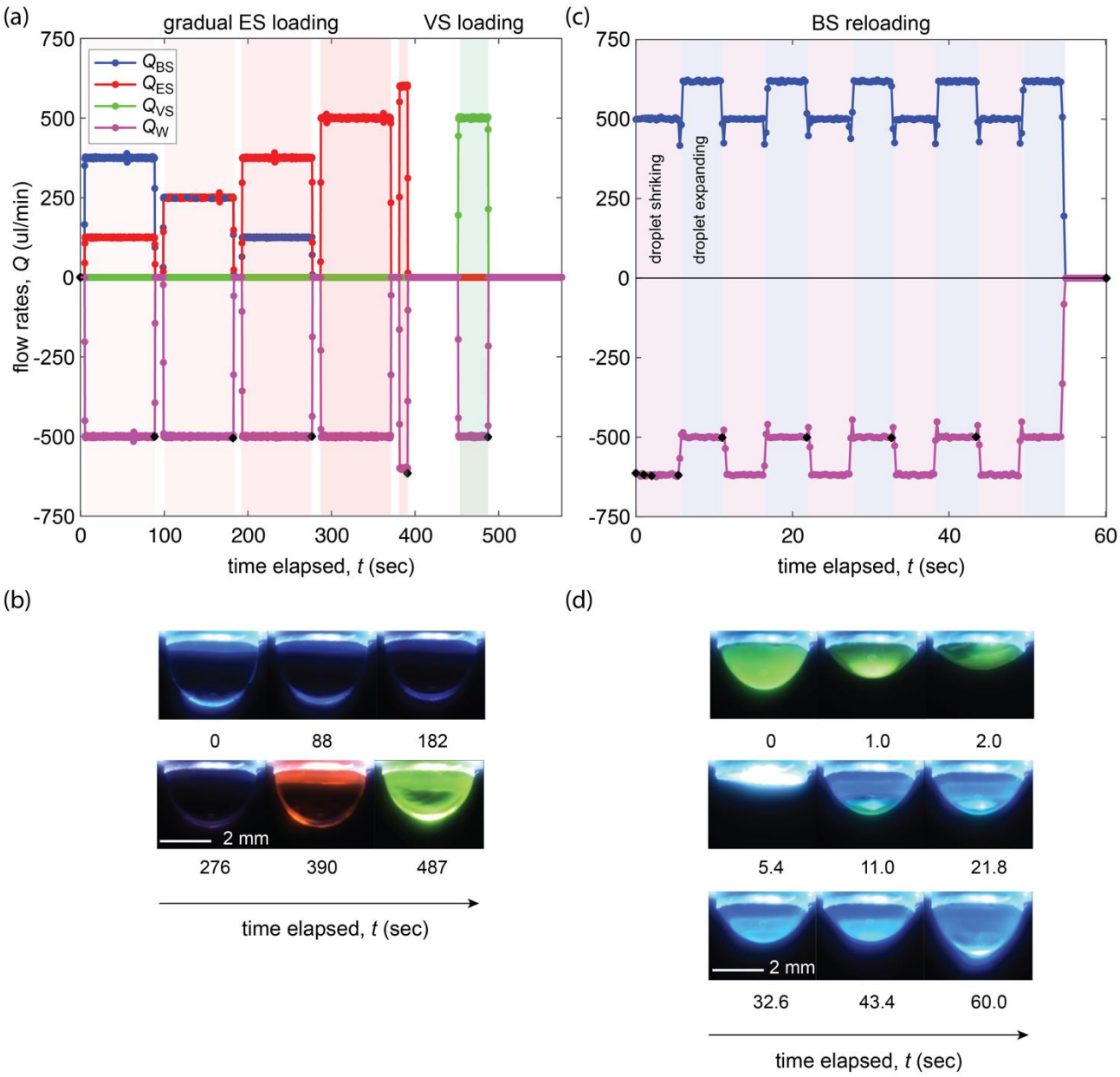

Fig. S13 Demonstration of modalities for gradual cryoprotectant loading, and cryoprotectant rinsing. a) Flow rates for gradual cryoprotectant loading for basic (Q_{BS}), equilibration (Q_{ES}), and vitrification solutions (Q_{VS}) dispensed (Q>0) into hanging droplet. Consecutive red bands indicate increasing ratios Q_{ES}/Q_{BS}. To keep a constant droplet volume, an equal amount of flow rate Q_W is aspirated (Q<0) from hanging droplet into waste. b) Images of droplet corresponding at time elapsed denoted by black diamonds in (a). c) Flow rates for rinsing VS from droplet by reloading BS via oscillations of droplet volume (**Video S5**). Oscillating the droplet volume facilitated switching VS with BS, where the latter has lower density (**Table. 1**). Magenta and blue bands indicate alternating Q_{BS}/Q_{VS} ratios that cause droplet to iteratively expand and shrink. d) Images of droplet corresponding at time elapsed denoted by black diamonds in (c).

Scaling analysis for estimating probability of cavitation

When unloading a given egg from the hanging droplet using the Cryoloop, a small portion of liquid gets detached from the hanging droplet, and forms a new interface around the Cryoloop containing egg. Liquid breakup could cause cavitation, leading to cell damage during this process. We never experimentally observed generation of air bubbles (cavitation) when we unloaded the egg from the air-liquid interface using the Cryoloop. We also never saw disruption of cell morphology in the Cryoloop, apart from the expected shrinkage in the event of overexposure to VS.

To explain this experimental observation, we calculated a scaling number to estimate the probability of cavitation in our system. We thus calculated the Cavitation number Ca as: $Ca = 2(P - P_{\mathrm{v}})/\rho V_{un}^2$ where low value ($Ca \ll 1$) indicates high probability of cavitation. In our system, the pressure P is equal to that of atmosphere ($P = P_{\mathrm{atm}} = 10^5$ Pa), P_{v} and ρ are respectively the vapor pressure and density of Vitrification Solution (VS) that is loaded on the droplet before the unloading of the egg. V_{un} is the characteristic velocity at which the liquid gets detached from the liquid-air interface to form a film around Cryoloop. VS has three components (**Table. 1**), which are less volatile than water at room temperature ($P_{\mathrm{v,H_2O}} = 3.17\mathrm{kPa}$) such as DMSO ($P_{\mathrm{v,DMSO}} = 0.0747\ \mathrm{kPa}$), Ethylene Glycol ($P_{\mathrm{v,H_2O}} = 0.008\ \mathrm{kPa}$) and Sucrose ($P_{\mathrm{v,Sucrose}}$ practically zero). In the interest of a scaling argument, we took the more volatile (thus more cavitation-prone) scenario in which the vapor pressure of VS is equal to that of water ($P_{\mathrm{v}} = P_{\mathrm{v,H_2O}} = 3.17\ \mathrm{kPa}$) while the density is equal to that of VS ($\rho = \rho_{\mathrm{VS}} = 1.095\ \mathrm{g/cm^3}$). During the unloading of the egg from the droplet using the Cryoloop, we estimated the liquid surface retraction time to be of the order 10 ms based on previous literature studying retraction dynamics (1). With a retraction distance of 5mm, we calculated: $Ca \cong 700$ which indicates practically zero probability of cavitation and is consistent with our experimental observation of absence of bubbles during unloading of the egg.

Measurements on food dyes

We used food dye from Ideallife, which contains FDA-approved water-soluble dye such as Red 40, Blue 1, and Green 3. In our vitrification experiments, we added 20 µl of concentrated food dye in 10 ml of solutions, making 0.2%v/v food dye solutions, corresponding to 500X dilutions. To calculate the molar concentration of our dyes in our solutions, we made 50X dilutions ($V_{dye} = 20\text{ul dye}, V_w = 980\text{ul water}$) of our concentrated dye, and measured the mass of well-defined volume aliquots. In particular, we measured masses between 903 and 905 mg of 900 ul volumes, corresponding to maximum density of $\rho_{50X} = 1.005\text{ g/ml}$. Given that the density of water is $\rho_w = 0.998\text{ g/ml}$, we calculated the maximum density $\rho_{i,dye}$ of our initial dye solution from $\rho_{50X} = (\rho_{i,dye} V_{i,dye} + \rho_w V_w)/V_t$, as $\rho_{i,dye} = 1.376\text{ g/ml}$. Thus in 1 ml solution, we have $m_{dye} = 378\,mg$. Given that molecular weight of dyes are $M_{\text{w}} = 500\ to\ 900\text{ g/mol}$ (5), for mean molecular weight we can estimate around $c_i = 0.5\text{M}$. Having a 500X dilution, means that we have a maximum of $c = 1\text{ mM}$ in our solutions.

In aqueous solutions (similar to our Basic solution) viscosity has been shown to linearly increase up to 40% at dye concentrations of $1 - 100\text{ mM}$ (6). Since our concentration is at maximum 1mM, we assumed that would have negligible effect on viscosity of BS solution. Similarly, we do not expect the density of the solution to be affected by the addition of the dye. In aqueous solutions with significant percentage of organic solvents (such as Ethelene glycol l, similar to our Equilibration and Vitrification solutions which have 7.5% to 15% v/v), viscosity has also been known to increase. Indicatively, there is a 20% increase in viscosity for 10-20%v/v solutions of Ethylene Glycol at dye concentration of 100mM (7). Given that our solutions have concentrations up to 1mM, we assumed that the effects of dyes on viscosity (as well as density) are negligible.

In our COMSOL simulations we used the fluid values (**Table. 1**) assuming negligible effect of dyes due to their smaller molar concentrations (≤1mM). Given the high concentrations of ethylene glycol (15%) dimethyl sulfoxide (15%), and sucrose (1M) in the cryoprotectant, we assumed that the fluid's density and viscosity are predominantly determined by these components.

Our scaling analysis (**Fig. S5b,c**) shows that our system operates at an intermediate Reynolds regime ($Re = 20 - 400$), thus we anticipate that changes of viscosity (e.g. 20%) from a scaling point of view will keep the operation in the same Re regime, thus the times τ for liquid exchange will stay in the same order of magnitude of 5-20sec (**Fig. 5**).

List of symbols

A Channel cross-section area
Ar Archimedes number
Bo Bond number
Ca Cavitation number
D Diffusion coefficient
d Egg diameter
F_{B} Buoyancy force
F_G Gravity force
F_{σ} Interface tension force
g gravitational constant
L Hanging drop characteristic length
m mass of solution in droplet
NA Numerical aperture
P_{atm} Atmospheric pressure
P_{in} Inlet pressure
P_{out} Outlet pressure
P_{v} Vapor pressure
Re Reynolds number
t Channel thickness
V_{a} Advection velocity, characteristic flow velocity
V_{s} Sedimentation velocity
V_{d} Droplet volume
w Channel width
σ Interface tension
ρ liquid density
ρ_{e} Egg density
τ_{a} Advection time scale
τ_{D} Diffusion time scale
τ_{e} Liquid exchange time scale
τ_{s} Sedimentation time scale
μ Dynamic viscosity

subscripts for fluid properties (μ, ρ, σ, m) and for solutions
BS Basic Solution
ES Equilibration Solution
VS Vitrification Solution

subscripts for Channel cross-section area
s single channel
d double channel

Supplementary References

1. Wang, F.; Fang, T. Retraction dynamics of water droplets after impacting upon solid surfaces from hydrophilic to superhydrophobic. Physical Review Fluids 2020, 5 (3), 033604. DOI: 10.1103/PhysRevFluids.5.033604.
2. T.J Atherton, D.J. Kerbyson. "Size invariant circle detection." Image and Vision Computing. Volume 17, Number 11, 1999, pp. 795-803.
3. H.K Yuen, .J. Princen, J. Illingworth, and J. Kittler. "Comparative study of Hough transform methods for circle finding." Image and Vision Computing. Volume 8, Number 1, 1990, pp. 71–77.
4. Qiu Y, Chen X, Li Y, Chen WR, Zheng B, Li S, Liu H. Evaluations of auto-focusing methods under a microscopic imaging modality for metaphase chromosome image analysis. Anal Cell Pathol (Amst). 2013;36(1-2):37-44. doi: 10.3233/ACP-130077. PMID: 23629477; PMCID: PMC3748595.
5. National Library of Medicines, National Center for Biotechnology information, https://pubchem.ncbi.nlm.nih.gov/
6. Wang, Huan, Han Kong, Jie Zheng, Hui Peng, Chuangui Cao, Yong Qi, Kuanjun Fang, and Weichao Chen. 2020. "Systematically Exploring Molecular Aggregation and Its Impact on Surface Tension and Viscosity in High Concentration Solutions" *Molecules* 25, no. 7: 1588. https://doi.org/10.3390/molecules25071588
7. Yong Qi, Ruyi Xie, Aihong Yu, Mohd Nadeem Bukhari, Liyuan Zhang, Chuangui Cao, Hui Peng, Kuanjun Fang* and Weichao Chen 2020 “Effect of ethylene glycol and its derivatives on the aggregation properties of reactive Orange 13 dye aqueous solution, DOI: 10.1039/D0RA06330D (Paper) *RSC Adv.*, 2020, **10**, 34373-34380